Manipulating Charge Density in Nanofluidic Membranes for Optimal Osmotic Energy Production Density

Changjia Zhu, Weipeng Xian, Yanpei Song, Xiuhui Zuo, Yeqing Wang, Shengqian Ma,* and Qi Sun*

Uncontrolled mixing remains the primary hurdle impeding the practical application of reverse electrodialysis (RED) to harvest Gibbs free energy in the form of salinity gradients. Improving the permselectivity of membranes is therefore essential, with ionic density being one of the most critical factors. Herein, it is systematically investigated how the charge population in nanofluidic membranes affects the ionic charge separation and consequently the accompanying power density. To establish this relationship, the effect of the ionic density is decoupled from the impact of pore structure using a multivariate strategy to construct covalent-organic-framework-based membranes, in which the content of ionic sites can be precisely manipulated from 0 to 0.18 C m^{-2}, a range that has rarely been experimentally explored. Beyond the region reported (0.002–0.06 C m^{-2}), wherein increasing pore surface charge density of the membrane enhances permselectivity and leads to a greater osmotic voltage, a sharp volcano-like curve is observed. The optimal membrane affords record-high power outputs among membrane systems, one order of magnitude higher than the value set for commercialization. The study provides insights into the impact of ionic density of the membrane on osmotic energy harvesting that can guide RED stack design to advance sustainable energy generation from natural salinity gradients.

1. Introduction

Limited resource availability and growing energy demand have generated interest in utilizing nonconventional energy. An enormous amount of energy is available in the form of the salinity difference between seawater and freshwater, with a total estimated power of 1.4–2.6 TW, ranking it as the second-largest marine-based energy source. Nevertheless, it remains an untapped resource.[1,2] Numerous technologies have been developed to capture this energy, among which reverse electrodialysis (RED) holds great promise because it can directly discharge the stored Gibbs free energy.[3,4] The central part of RED salinity batteries consists of ionic membranes which screen ions, causing a preferential accumulation of charges at the channel ends and thus generating a transmembrane potential. Improving the permselectivity of the membranes can restrain the unwanted entropy generation from nonselective mixing.[5,6] The charge population is a crucial variable controlling the selectivity of ion transport through nanochannels.[7–13] The permselectivity of ionic membranes increases as the number of ionic sites increases, which is accompanied by a corresponding increase in the osmotic power generation efficiency.[14–33] The intrinsic charge density of most synthetic systems is lower than 0.06 C m^{-2}, although it is claimed that the surface charge density of some materials can reach ≈1 C m^{-2}, by adjusting the solution pH (Table S1, Supporting Information). The fluid mechanics in high-ionic-density regimes under near-neutral conditions is largely unexplored because conventional ionic membrane preparation does not allow varying the distribution of ionic sites without simultaneously changing the pore structure and swellability.[34] There has been a small number of theoretical studies attempting to correlate the surface charge distribution of membranes to their power output efficiency, but their experimental verification remains debatable.[35]

To answer these questions, the main challenge comes from the significant difficulties related to the predictability and controllability of decorating ionic sites in a defined nanospace. Insight from reticular chemistry offers promising solutions for manipulating the spatial distribution of charged sites while deconvoluting the pore structure.[36] Covalent organic frameworks (COFs) are promising candidates for this task because they can be used to synthesize well-defined nanochannels and tunable interior structures that allow for ion permselectivity. The bottom-up self-assembly of reticular materials enables the precise placement of functionality with predetermined distances with respect to one another within a framework

C. Zhu, W. Xian, X. Zuo, Q. Sun
Zhejiang Provincial Key Laboratory of Advanced Chemical Engineering
Manufacture Technology
College of Chemical and Biological Engineering
Zhejiang University
Hangzhou 310027, China
E-mail: sunqichs@zju.edu.cn
C. Zhu, Y. Song, S. Ma
Department of Chemistry
University of North Texas
1508 W Mulberry St, Denton, TX 76201, USA
E-mail: shengqian.ma@unt.edu
Y. Wang
Key Lab of Applied Chemistry of Zhejiang Province
Department of Chemistry
Zhejiang University
Hangzhou 310028, China

**ADVANCED
SCIENCE NEWS**
www.advancedsciencenews.com

**ADVANCED
FUNCTIONAL
MATERIALS**
www.afm-journal.de

architecture necessary for elucidating the correlation between ionic density and output power efficiency.[37–46] Concurrently, the rigid framework and regular intrinsic porosities of COFs can prohibit swelling and facilitate ion diffusion to increase the flux, which is a great improvement over traditional ionic membranes.

Thus, we reasoned that the systematic charge modulation of a COF system could facilitate a fundamental investigation of the relationship between the charge density, ion permselectivity, and output power efficiency. To establish such correlations, we employed a multivariate (MTV) strategy to vary the charge population while maintaining an identical structure.[47] We found that the ion transport process has a highly complex response to charge variations. A sharp volcano-like curve was discovered when optimizing the content of ionic sites in the COF-based membranes, which disagrees with the previous results that the RED efficiency is positively correlated with the membrane charge density. When assembled into RED stacks, the best membrane achieved a power density of up to 54.0 W m^{-2} at a 50-fold salinity gradient, which is typical at river mouths. This surpasses the performance of any previously reported membrane system and exceeds the commercialization benchmark by more than one order of magnitude (Table S1, Supporting Information). Our work therefore has immense practical implications for identifying an optimal range of ionic density for achieving maximum energy conversion using a nanofluidic device, rather than superfluously aiming for ultrahigh charge populations.

2. Result and Discussion

To implement this strategy, we selected the COF constructed by triformylphloroglucinol (Tp) and terephthalohydrazide as the platform to develop nanofluidic membranes because the resulting material not only possesses high crystallinity and salinity tolerance but also exhibits excellent functional compatibility, which provides an opportunity to control the charge population in one material.[48,49] To promote the homogeneous distribution of ionic sites, we selected 2,2′-((2,5-di(hydrazinecarbonyl)-1,4-phenylene) bis(oxy))bis(N,N,N-trimethylethan-1-aminium) iodide (BTA) and 2,5-bis(2-(dimethylamino)ethoxy)terephthalohydrazide (BTH) with similar polarity as ionic and nonionic moieties, respectively, to adjust the charge density by varying their ratio during membrane synthesis. Interface polymerization was adopted to obtain membranes in which the organic solution containing Tp was layered onto an acetic acid aqueous solution of hydrazides. The resulting membranes are denoted as COF-BTA$_x$BTH$_y$ (x and y refer to the molar proportions of BTA and BTH used in the synthesis of the membrane, respectively; **Figure 1**). The powder X-ray diffraction (PXRD) patterns of COF-BTA$_x$BTH$_y$ displayed isostructural features comparable to the simulated pattern of the $P6/m$ model, thereby demonstrating their crystalline structure, in which the 2D sheets are packed in eclipsed AA stacking, yielding a continuous nanometer-scale path for ion travel (Figure S1, Supporting Information). The Brunauer–Emmett–Teller (BET) surface area of COF-BTA$_1$BTH$_1$ calculated from the N$_2$ adsorption isotherm was 309 m^2 g^{-1}, and the average pore size distribution derived from nonlocal density functional theory (NLDFT) was 2.0 nm, which is in line with the pore size calculated from the crystal simulation considering eclipsed AA stacking (Figure S3, Supporting Information). The PXRD pattern and N$_2$ sorption isotherms of COF-BTA$_1$BTH$_1$ following immersion in 3 M NaCl for at least one week closely matched that of the pristine material, revealing its high salt tolerance, which is critical to achieving long-term stability in RED (Figure S2, Supporting Information). The appearance of a strong iodine signal in the X-ray photoelectron spectroscopy (XPS) results for COF-BTA$_x$BTH$_y$ confirmed the successful incorporation of the ionic moieties (Figure S4, Supporting Information).
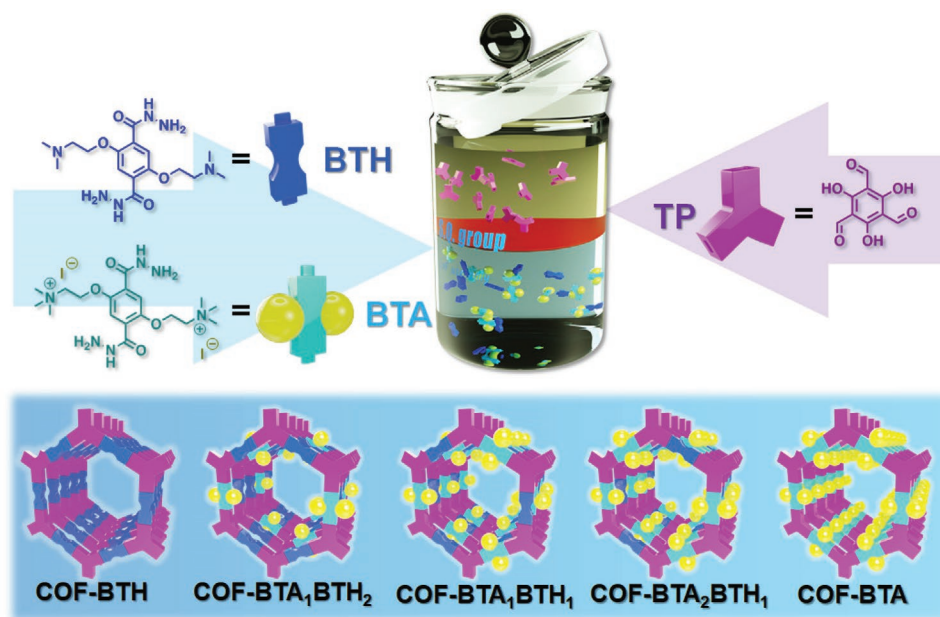

Figure 1. Fabrication processes for COF-based nanofluidic membranes with varied charge densities.

The N 1s XPS profiles recorded from free-standing COF-BTA$_x$BTH$_y$ membranes revealed that the relative surface areas of N 1s originating from quaternary ammonium increased proportionally as the molar proportion of BTA increased (Figure S5, Supporting Information). The exact contents of iodine species were estimated using an electron probe microanalyzer (EPMA) to be 0%, 11.0%, 15.8%, 21.0%, and 33.2% for COF-BTH, COF-BTA$_1$BTH$_2$, COF-BTA$_1$BTH$_1$, COF-BTA$_2$BTH$_1$, and COF-BTA, respectively, demonstrating a positive correlation between the stoichiometry of the starting materials and the actual linker ratios in the resulting COF membranes (Table S2, Supporting Information). The homogeneous distribution of ionic sites in these membranes was validated by elemental mapping attached to EPMA (Figure S6, Supporting Information).

To increase the operability, we grew the COF active layers on a polyacrylonitrile (PAN) ultrafiltration membrane (Figure S7, Supporting Information). The color of the resulting membrane changed from dark red to orange as the BTA proportion increased (Figure S8, Supporting Information). No absorbance from the aldehyde C=O (1640 cm^{-1}) and hydrazide primary N–H (3270 cm^{-1}) stretching modes from the starting materials were detected in the Fourier-transform infrared spectra of the resulting membranes, suggesting the occurrence of the condensation reaction (Figure S9, Supporting Information). Additional evidence for the establishment of an extended framework was provided by the formation of amide linkages (1582 cm^{-1}).[48,49] The quaternary ammonium absorbance of C–N (1406 cm^{-1}) increased with the BTA content, providing another line of evidence for the varied ionic densities in the resulting membranes (Figure S9, Supporting Information). The Zeta potentials of the COF-BTA$_x$BTH$_y$/PAN membranes were less negative than that of the pristine PAN, with the value increasing with the BTA proportion, indicating that there are more positively charged struts in the resulting active layers (Figure S10, Supporting Information). The bipolar nature of the membrane assists in suppressing concentration polarization and promoting ion transport.[50] The water contact angle measurements indicate that the membranes are hydrophilic, with values decreasing from 51.2° to 36.1° in response to the increase in BTA content (Figure S11, Supporting Information). Scanning electron microscopy (SEM) images of COF-BTA$_x$BTH$_y$/PAN revealed continuous film surfaces of ≈300 nm thickness that contoured the underlying PAN support (Figures S12–S17, Supporting Information). Tests for membrane leakage were carried out by dye molecule exclusion (rhodamine B, 20 ppm aqueous solution). No UV–vis signal was detected for the positively charged rhodamine B in the filtrate following dead-end filtration (Figure S18, Supporting Information). Collectively, these isostructural COF-based membranes allowed us to demonstrate the impact of the charge population on RED performance without interference from the local structure of the membrane, which is unachievable in traditional ionic membranes.

Encouraged by these characterization results, we proceeded to investigate the ion transport behavior across the membrane. All of these experiments involve a conductive cell in which the membrane to be studied separates two symmetric KCl aqueous solutions having concentrations varying from 0.01×10^{-3} to 3 M (**Figure 2**a). Current–voltage (I–V) plots recorded using Ag/AgCl electrodes for COF-BTA$_x$BTH$_y$/PAN shows linear ohmic behavior (Figure S19, Supporting Information). All the plots of the conductivity against the KCl concentration for COF-BTA$_x$BTH$_y$/PAN exhibited a plateau with a small but gradual increase with increasing electrolyte concentrations, which is a characteristic of surface-charge-governed transport. At high ionic concentrations, the conductivity increased linearly with electrolyte concentration, approaching bulk behavior. Close analyses of the data show that at low concentrations, the conductivity of the membranes increased with the number of ionic sites (Figure 2b). This may occur because at low salt concentrations, surface conduction is dominant over bulk conduction, which is determined by the availability of charged sites. Hence, a saturation in conductance is noted at elevated values of the surface charge density. The COF-BTH/PAN nanochannels were positively charged in the aqueous KCl solution because the isoelectric point of the amine species is higher than 7 (for the calculation of charge density of the COF membranes, see details in Table S3 in the Supporting Information). Furthermore, these membranes exhibited similar transition concentrations between the surface-charge-governed and bulk-behavior regimes, validating that these COFs are isostructural.[51] Using the Debye–Hückel approximation, the channel size of COF-BTA$_x$BTH$_y$ was estimated to be ≈2 nm, which is
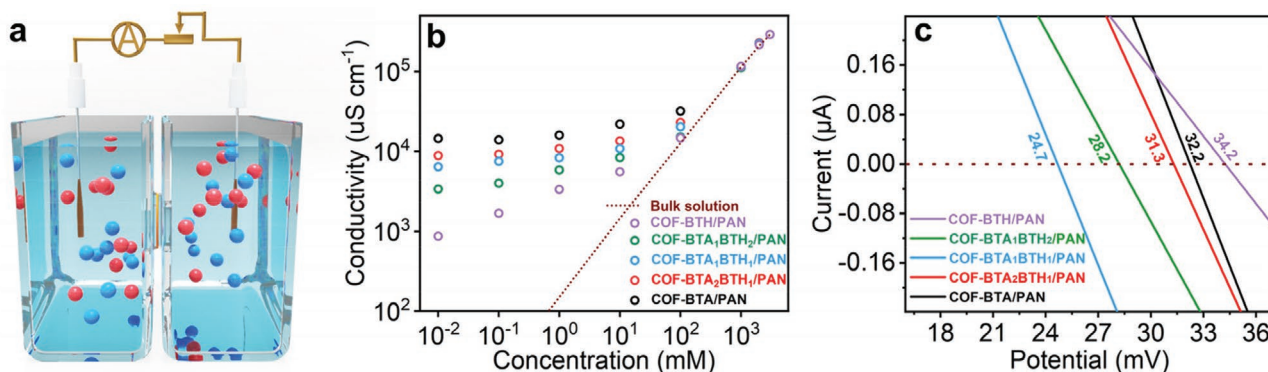

Figure 2. Ionic transport properties of COF-BTA$_x$BTH$_y$/PAN. a) Schematic of the experimental setup for measuring the transmembrane ionic transport (cation, blue; anion, red). b) Conductivity versus KCl concentration for COF-BTA$_x$BTH$_y$/PAN. The ionic conductance deviates from the bulk value (dashed line) in the low-concentration region, indicative of surface-charge-governed ion transport. c) I–V curves recorded for COF-BTA$_x$BTH$_y$/PAN under KCl solutions with a concentration gradient of 50×10^{-3} M/0.1×10^{-3} M.

in agreement with the simulated values (Table S4, Supporting Information). These features facilitate rigorous comparisons to establish correlations between the number of charged sites and their capability in harvesting salinity gradient energy.

To determine the charge selectivity of COF-BTA$_x$BTH$_y$/PAN, the membrane was mounted between various asymmetric electrolyte solutions (50×10^{-3} M/0.1×10^{-3} M, KCl, NaCl, LiCl, or MgCl$_2$,), with the COF active layer facing the high-concentration side. The positive x-intercepts (V_r) of the current–voltage ($I–V$) plots provided simple visual evidence that these membranes can screen the transport of cations while favoring that of anions (Figure S20, Supporting Information). The permselectivity of anion to cation was calculated to be 181, 206, 246, and 216 for KCl, NaCl, LiCl, and MgCl$_2$, respectively, using the Goldman–Hodgkin–Katz equation, as exemplified by COF-BTA$_1$BTH$_1$/PAN (see details in the Supporting Information).[52] Notably, the COF-BTA$_x$BTH$_y$/PAN membranes exhibited different permselectivities. COF-BTA$_1$BTH$_1$/PAN, which possessed a moderate charge density, showed the highest $P(Cl^-)/P(K^+)$ among the membranes tested, implying a potential discrepancy in the generation of osmotic potential (Figure 2c). The observed inconsistent Cl$^-$ selectivity for various electrolytes is because of the different mobility for the cations relative to Cl$^-$, decreasing in the order of K$^+$ > Na$^+$ > Li$^+$ > Mg^{2+}.

Since coion leakage is the dominant detrimental factor affecting the RED power density, we subsequently evaluated the ionic charge separation performance of these membranes. To this end, KCl solutions having a wide range of concentration gradients were positioned across COF-BTA$_x$BTH$_y$/PAN. To exclude the contribution of the redox potential of Ag/AgCl electrodes derived from the inequable potential drop at the electrode–electrolyte interface, a home-built conductive cell with a pierced membrane separating the three fluidic reservoirs was used, in which the high-concentration solution chamber was separated from two low-concentration solution chambers by the COF membrane and PAN, respectively (**Figure 3**a). The use of PAN is mainly based on the consideration that it can segregate two compartments, thereby preventing the rapid mixing of the solutions, and it is nearly nonselective, facilitating the investigation of the performance of COF. KCl solutions having concentrations varying between

0.1×10^{-3} and 0.5 M were used. We set the concentration of the side reservoirs to 0.1×10^{-3} M, and gradually increased the concentration of the central chamber from 0.5×10^{-3} to 0.5 M. The open-circuit voltage (V_{oc}) and short-circuit current (I_{sc}) can be read directly from the intercepts of the collected $I–V$ plots. Figure S21 in the Supporting Information shows the plots of V_{oc} and I_{sc} versus KCl concentration gradients. The calculated output power, $P \propto V_{oc} \times I_{sc}$, revealed that the corresponding values increased when the salt concentration gradient increased from 0.5×10^{-3} M/0.1×10^{-3} M to 50×10^{-3} M/0.1×10^{-3} M, but decreased when the salt concentration was further increased to 0.5 M/0.1×10^{-3} M (Figure 3b). COF-BTA/PAN, which exhibited the highest charge density among the membranes tested, did not afford the highest V_{oc} and I_{sc} values by a wide margin. This was counterintuitive because previous experimental results indicated that increasing the charge density of a specific channel can increase the power generation efficiency. In comparison, COF-BTA$_1$BTH$_1$/PAN, despite possessing a much lower charge density, exhibited the highest values. Considering that these membranes are constructed by isostructural COFs having similar thicknesses, the impact of the dynamic resistance of the membrane can be excluded. Therefore, the discrepancy in energy conversion could reasonably be attributed to the variation in ionic density (Figure 3b). Essentially, the V_{oc} originates from the differences in the diffusive fluxes of anions and cations across the membrane, which can be expressed quantitatively by the transference number (t_-). To evaluate the relationship between the charge density of the membrane and its power generation efficiency, we plotted the t_- values versus concentration gradient. Due to electric double layer compression along with the increase of ionic strength, the permselectivity deteriorates and thus the t_- values show a trend of decrease with concentration gradient increases. It is demonstrated that COF-BTA$_1$BTH$_1$/PAN exhibits higher t_- values than those of other membranes, especially in the high-salt-concentration region, which is consistent with the experimental results obtained above. At the salt concentration gradient of 0.5 M/0.1×10^{-3} M, COF-BTA$_1$BTH$_1$/PAN can still offer a t_- value of 0.92, which assists in curbing the undesired entropy production from the uncontrolled mixing of high-salinity-gradient solutions (Figure 3c).
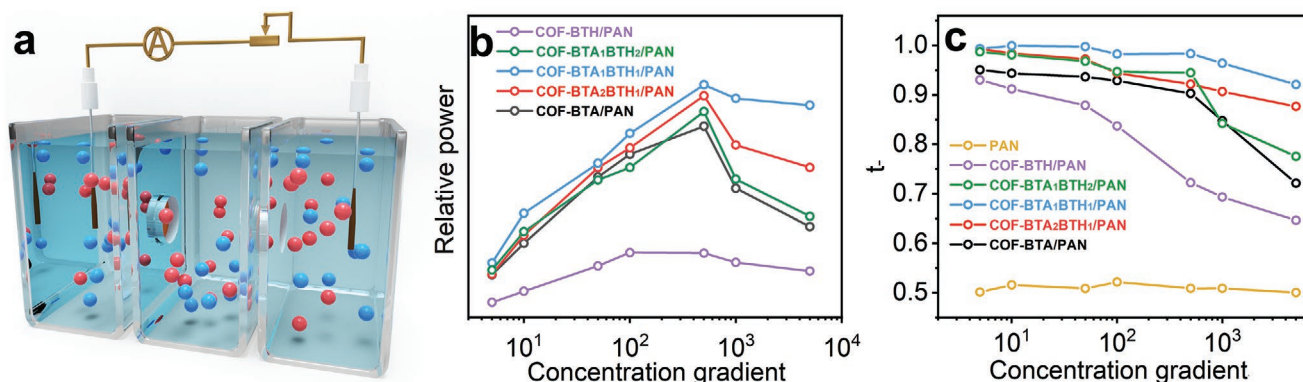

Figure 3. Investigation of ion permselectivity. a) Schematic of the experimental setup used to evaluate the permselectivity of the membranes (cation, blue; anion, red). b) Relative output power as a function of KCl concentration gradients over COF-BTA$_x$BTH$_y$/PAN. c) Plots of transference number (t_-) versus various KCl concentration gradients across COF-BTA$_x$BTH$_y$/PAN.

ADVANCED
SCIENCE NEWS
www.advancedsciencenews.com

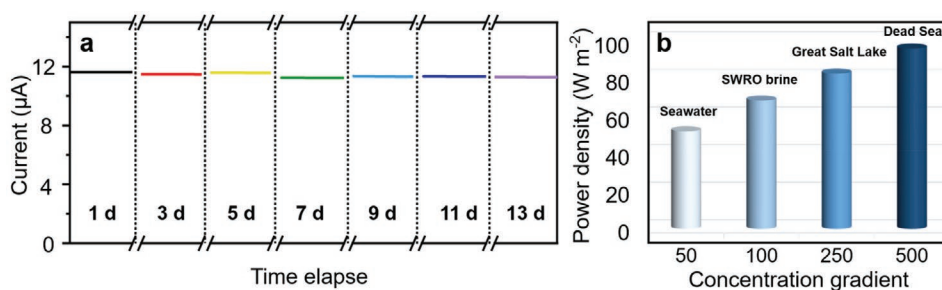ADVANCED
FUNCTIONAL
MATERIALS
www.afm-journal.de

The excellent permselectivity of COF-BTA$_x$BTH$_y$/PAN paved the way for osmotic energy harvesting. Understanding the impact of the surface charge density on the power generation efficiency was further facilitated by assembling the membranes into a RED stack that is more practicable. Nafion212 was used as the cation-selective membrane paired with COF-BTA$_x$BTH$_y$/PAN. River mouths are potential locations for exploiting osmotic energy sustainably, because perpetually freshwater mixes with seawater at these locations. Therefore, a concentration gradient of 10×10^{-3} M/0.5 M NaCl was applied between the three compartments to approach real-world values of the ion concentrations of river water and seawater, respectively, at river mouths. In this device, the cations migrated through Nafion212 toward the anode, resulting in an increase in electrode potential, whereas the anions transported preferentially through COF-BTA$_x$BTH$_y$/PAN toward the cathode, resulting in a decrease in the electrode potential. The complementary ionic charge produced an electrochemical potential difference between the two electrodes. The harvested salinity-gradient energy was output to an external circuit to furnish an electronic load resistor (R_L). The current density in the external circuit decreased as the load resistance increased; the output power density, calculated as $P = I^2 \times R_L$, reached a maximum value when the intermediate resistance was equal to the membrane resistance (at around 1×10^4 Ω; **Figure 4**a; Figure S22, Supporting Information). It was found that the content of ionic sites had a significant influence on the osmotic energy conversion. The plot of the power density as a function of ionic density in COF-BTA$_x$BTH$_y$/PAN displayed a trend of increase

followed by decrease, with COF-BTA$_1$BTH$_1$/PAN being optimal, exhibiting a value of 51.9 W m^{-2} (Figure 4b).

To understand the origin of this intriguing pattern, we used numerical calculations to explore the nature of this anion permselectivity. The estimated ionic concentrations in the nanochannel can be used to rationalize the experimental results. Although the Cl$^-$ concentration was much higher than the Na$^+$ concentration for all the membranes evaluated, a clear dependence on the charge density was evident (Figure 4c). The plot of the concentration ratio of Cl$^-$ and Na$^+$ versus charge density close to the channel aperture displayed in Figure 4d reveals distinct differences, showing a volcano-like curve with the maximum appearing at a charge density of 0.094 C m^{-2}. Accordingly, the charge density for maximum power output was calculated to be 0.094 C m^{-2}. We rationalized these trends using concentration polarization, a phenomenon caused by solute depletion and enrichment occurred at the channel apertures. As the surface charge density increases, the concentration polarization effect becomes more significant, which in turn results in an appreciable decrease in the effective salinity ratio.[53] These simulation results suggest that the energy conversion performance of COF-BTA$_x$BTH$_y$/PAN can be further optimized by adjusting the surface-charge density, as the charge densities in COF-BTA$_1$BTH$_1$/PAN and COF-BTA$_2$BTH$_1$/PAN are 0.085 and 0.103 C m^{-2}, respectively. To confirm the reliability of the above analysis, we synthesized COF-BTA$_3$BTH$_2$/PAN having a charge density close to 0.094 C m^{-2} (0.092 C m^{-2}), which afforded a power density of 54.0 W m^{-2}, which is consistent with the calculation results (Figures S23 and S24, Supporting Information). Remarkably, this
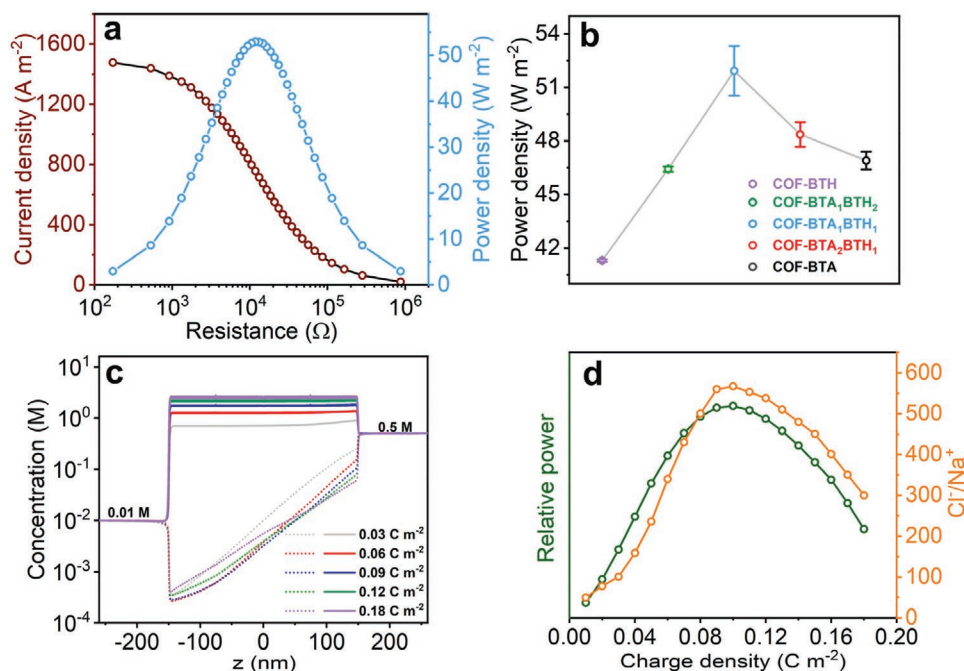
Figure 4. High-performance osmotic energy conversion and numerical simulation. a) The power was output to an external circuit to supply an electronic load. The diffusion current decreased with increasing load resistance, and the output power reached its peak at ≈12 kΩ, as exemplified by COF-BTA$_1$BTH$_1$/PAN. b) The maximum output power density was obtained using a pair of RED stack coupled by COF-BTA$_x$BTH$_y$/PAN and Nafion212; the error bars indicate the average standard deviation for all points. c) Numerical simulation of the impact of charge density on the Na$^+$ (dashed line) and Cl$^-$ (solid line) distribution in the nanochannels and d) plots of the concentration ratio of Cl$^-$ and Na$^+$ close to the channel aperture, and output power versus charge density for a single channel.

**ADVANCED
SCIENCE NEWS**
www.advancedsciencenews.com

**ADVANCED
FUNCTIONAL
MATERIALS**
www.afm-journal.de

Figure 5. Stability evaluation and salinity gradient energy harvesting. a) Time series plots of current versus time (I–T) for the RED device coupled by COF-BTA$_1$BTH$_1$/PAN and Nafion212 by mixing artificial river water and seawater. b) The theoretically extractable energy is from the mixing of a dilute stream with saline solutions from four sources. At increased salinity gradients, the output power density increases, and reaches a maximum at the 500-fold salinity gradient between the Dead Sea and freshwater. The lengths of error bar for seawater, SWRO brine, Great Salt Lake, and Dead Sea are 1.39, 1.92, 1.78, and 2.06 W m^{-2}, respectively.

value exceeds that of all multipore membrane systems reported to date, and is more than one order of magnitude higher than the commercialization benchmark (5 W m^{-2}). The corresponding energy conversion efficiency of the RED device was calculated to approach 33%. Given that the t_+ value for Nafion212 under the NaCl concentration gradient of 10×10^{-3} м/0.5 м is 0.91 (Figure S25, Supporting Information), the efficiency of COF-BTA$_1$BTH$_1$/PAN is thus calculated to be 39.8%.

Long-term stability is essential for reducing the costs and aiding the proliferation of salinity-gradient energy production plants. To evaluate the cycle stability, COF-BTA$_1$BTH$_1$/PAN was selected as a representative sample and repeatedly used in a 10×10^{-3} м/0.5 м NaCl RED system. A negligible decrease was observed in I_{sc} and V_{oc} over 13 days of operation (**Figure** 5a; Figure S26, Supporting Information).

In addition to the Gibbs free energy at river mouths, there is an enormous amount of energy inherent in the salinity difference between the saltwater and freshwater. To estimate the energy-conversion performance of COF-BTA$_1$BTH$_1$/PAN under these salinity gradients, the NaCl concentration in the side chambers was maintained at 10×10^{-3} м, while the salt concentration in the middle chamber was filled to model well-known salt lakes. The output power densities listed in Figure 5b increased with the salinity gradient, and a maximum power density of 95.9 W m^{-2} was achieved at the Dead Sea/river water salinity gradient.

3. Conclusion

The present work describes an experimental investigation of the impact of the charge density of COF-based membranes on their RED performance, culminating in the development of highly efficient membranes for harvesting salinity-gradient energy. A more complex relationship was discovered by plotting the ionic density against the output power, which was inconsistent with existing knowledge. The experimental findings were validated and explained by numerical simulations. The derived structure–property relationships were further leveraged to tailor the charge density of the membranes to optimize their RED efficiency. Our study also highlights that COFs are a tailorable platform for providing mechanistic insight into ionic charge separation, and are therefore crucial materials for guiding the design of novel membranes.

Supporting Information

Supporting Information is available from the Wiley Online Library or from the author.

Conflict of Interest

The authors declare no conflict of interest.

Data Availability Statement

The data that support the findings of this study are available from the corresponding author upon reasonable request.

[1] Y. Zhou, L. Jiang, *Joule* **2020**, *4*, 2244.
[2] Y. Zhu, K. Zhan, X. Hou, *ACS Nano* **2018**, *12*, 908.
[3] J. Veerman, M. Saakes, S. J. Metz, G. J. Harmsen, *Environ. Sci. Technol.* **2010**, *44*, 9207.
[4] Y. Zhao, J. Wang, X.-Y. Kong, W. Xin, T. Zhou, Y. Qian, L. Yang, J. Pang, L. Jiang, L. Wen, *Natl. Sci. Rev.* **2020**, *7*, 1349.
[5] G. Z. Ramon, B. J. Feinberg, E. M. V. Hoek, *Energy Environ. Sci.* **2011**, *4*, 4423.
[6] B. E. Logan, M. Elimelech, *Nature* **2012**, *488*, 313.
[7] J. Lu, H. Zhang, J. Hou, X. Li, X. Hu, Y. Hu, C. D. Easton, Q. Li, C. Sun, A. W. Thornton, M. R. Hill, X. Zhang, G. Jiang, J. Z. Liu, A. J. Hill, B. D. Freeman, L. Jiang, H. Wang, *Nat. Mater.* **2020**, *19*, 767.

**ADVANCED
SCIENCE NEWS**
www.advancedsciencenews.com

**ADVANCED
FUNCTIONAL
MATERIALS**
www.afm-journal.de

[8] M. A. Shehzad, Y. Wang, A. Yasmin, X. Ge, Y. He, X. Liang, Y. Zhu, M. Hu, X. Xiao, L. Ge, C. Jiang, Z. Yang, M. D. Guiver, L. Wu, T. Xu, *Angew. Chem., Int. Ed.* **2019**, *131*, 12776.

[9] R. Tan, A. Wang, R. Malpass-Evans, R. Williams, E. W. Zhao, T. Liu, C. Ye, X. Zhou, B. P. Darwich, Z. Fan, L. Turcani, E. Jackson, L. Chen, S. Y. Chong, T. Li, K. E. Jelfs, A. I. Cooper, N. P. Brandon, C. P. Grey, N. B. Mckeown, Q. Song, *Nat. Mater.* **2020**, *19*, 195.

[10] Y. Xu, *Adv. Mater.* **2018**, *30*, 1702419.

[11] J. Wang, Z. Zhang, J. Zhu, M. Tian, S. Zheng, F. Wang, X. Wang, L. Wang, *Nat. Commun.* **2020**, *11*, 3540.

[12] E. T. Acar, S. F. Buchsbaum, C. Combs, F. Fornasiero, Z. S. Siwy, *Sci. Adv.* **2019**, *5*, eaav2568.

[13] W. Xin, C. Lin, L. Fu, X.-Y. Kong, L. Yang, Y. Qian, C. Zhu, Q. Zhang, L. Jiang, L. Wen, *Matter* **2020**, *4*, 737.

[14] X. Zhu, J. Hao, B. Bao, Y. Zhou, H. Zhang, J. Pang, Z. Jiang, L. Jiang, *Sci. Adv.* **2018**, *4*, eaau1665.

[15] R. Li, J. Jiang, Q. Liu, Z. Xie, J. Zhai, *Nano Energy* **2018**, *53*, 643.

[16] Y. Xu, Y. Song, F. Xu, *Nano Energy* **2021**, *79*, 105468.

[17] Z. Zhang, S. Yang, P. Zhang, J. Zhang, G. Chen, X. Feng, *Nat. Commun.* **2019**, *10*, 2920.

[18] L. Ding, D. Xiao, Z. Lu, J. Deng, Y. Wei, J. Caro, H. Wang, *Angew. Chem., Int. Ed.* **2020**, *59*, 8720.

[19] K. Xiao, P. Giusto, L. Wen, L. Jiang, M. Antonietti, *Angew. Chem., Int. Ed.* **2018**, *57*, 10123.

[20] H. Cheng, Y. Zhou, Y. Feng, W. Geng, Q. Liu, W. Guo, L. Jiang, *Adv. Mater.* **2017**, *29*, 1700177.

[21] Z. Zhang, L. He, C. Zhu, Y. Qian, L. Wen, L. Jiang, *Nat. Commun.* **2020**, *11*, 875.

[22] S. Hong, F. Ming, Y. Shi, R. Li, I. S. Kim, C. Y. Tang, H. N. Alshareef, P. Wang, *ACS Nano* **2019**, *13*, 8917.

[23] J. Feng, M. Graf, K. Liu, D. Ovchinnikov, D. Dumcenco, M. Heiranian, V. Nandigana, N. R. Aluru, A. Kis, A. Radenovic, *Nature* **2016**, *536*, 197.

[24] C. Chen, D. Liu, L. He, S. Qin, J. Wang, J. M. Razal, N. A. Kotov, W. Lei, *Joule* **2020**, *4*, 247.

[25] Y. Sun, T. Dong, C. Lu, W. Xin, L. Yang, P. Liu, Y. Qian, Y. Zhao, X.-Y. Kong, L. Wen, L. Jiang, *Angew. Chem., Int. Ed.* **2020**, *59*, 17423.

[26] Z. Zhang, P. Zhang, S. Yang, T. Zhang, M. Löffler, H. Shi, M. R. Lohe, X. Feng, *Proc. Natl. Acad. Sci. USA* **2020**, *117*, 13959.

[27] C.-Y. Lin, C. Combs, Y.-S. Su, L.-H. Yeh, Z. S. Siwy, *J. Am. Chem. Soc.* **2019**, *141*, 3691.

[28] C. Zhu, P. Liu, B. Niu, Y. Liu, W. Xin, W. Chen, X.-Y. Kong, Z. Zhang, L. Jiang, L. Wen, *J. Am. Chem. Soc.* **2021**, *143*, 1932.

[29] A. Siria, P. Poncharal, A.-L. Biance, R. Fulcrand, X. Blase, S. T. Purcell, L. Bocquet, *Nature* **2013**, *494*, 455.

[30] C. Chen, D. Liu, G. Yang, J. Wang, L. Wang, W. Lei, *Adv. Energy Mater.* **2020**, *10*, 1904098.

[31] G. Yang, W. Lei, C. Chen, S. Qin, L. Zhang, Y. Su, J. Wang, Z. Chen, L. Sun, X. Wang, D. Liu, *Nano Energy* **2020**, *75*, 104954.

[32] M. F. Jimenez-Solomon, Q. Song, K. E. Jelfs, M. Munoz-Ibanez, A. G. Livingston, *Nat. Mater.* **2016**, *15*, 760.

[33] Z. Zhang, L. Wen, L. Jiang, *Nat. Rev. Mater.* **2021**, *6*, 622.

[34] J. Pan, C. Chen, Y. Li, L. Wang, L. Tan, G. Li, X. Tang, L. Xiao, J. Lu, L. Zhuang, *Energy Environ. Sci.* **2014**, *7*, 354.

[35] Z. Zhang, X.-Y. Kong, K. Xiao, Q. Liu, G. Xie, P. Li, J. Ma, Y. Tian, L. Wen, L. Jiang, *J. Am. Chem. Soc.* **2015**, *137*, 14765.

[36] F. Haase, P. Hirschle, R. Freund, S. Furukawa, Z. Ji, S. Wuttke, *Angew. Chem., Int. Ed.* **2020**, *59*, 22350.

[37] M. S. Lohse, T. Bein, *Adv. Funct. Mater.* **2018**, *28*, 1705553.

[38] S. Kandambeth, K. Dey, R. Banerjee, *J. Am. Chem. Soc.* **2019**, *141*, 1807.

[39] Y. Jin, Y. Hu, W. Zhang, *Nat. Rev. Chem.* **2017**, *1*, 0056.

[40] K. Geng, T. He, R. Liu, S. Dalapati, K. T. Tan, Z. Li, S. Tao, Y. Gong, Q. Jiang, D. Jiang, *Chem. Rev.* **2020**, *120*, 8814.

[41] J. Dong, K. Zhang, X. Li, Y. Qian, H. Zhu, D. Yuan, Q.-H. Xu, J. Jiang, D. Zhao, *Nat. Commun.* **2017**, *8*, 1142.

[42] J. W. Colson, A. R. Woll, A. Mukherjee, M. P. Levendorf, E. L. Spitler, V. B. Shields, M. G. Spencer, J. Park, W. R. Dichtel, *Science* **2011**, *332*, 228.

[43] C. Yuan, X. Wu, R. Gao, X. Han, Y. Liu, Y. Long, Y. Cui, *J. Am. Chem. Soc.* **2019**, *141*, 20187.

[44] H. Yang, L. Yang, H. Wang, Z. Xu, Y. Zhao, Y. Luo, N. Nasir, Y. Song, H. Wu, F. Pan, Z. Jiang, *Nat. Commun.* **2019**, *10*, 2101.

[45] D. B. Shinde, G. Sheng, X. Li, M. Ostwal, A.-H. Emwas, K.-W. Huang, Z. Lai, *J. Am. Chem. Soc.* **2018**, *140*, 14342.

[46] Y. Li, Q. Wu, X. Guo, M. Zhang, B. Chen, G. Wei, X. Li, S. Li, L. Ma, *Nat. Commun.* **2020**, *11*, 599.

[47] Q. Sun, Y. Pan, X. Wang, H. Li, J. Farmakes, B. Aguila, Z. Yang, S. Ma, *Chem* **2019**, *5*, 3184.

[48] F. J. Uribe-Romo, C. J. Doonan, H. Furukawa, K. Oisaki, O. M. Yaghi, *J. Am. Chem. Soc.* **2011**, *133*, 11478.

[49] X. He, Y. Yang, H. Wu, G. He, Z. Xu, Y. Kong, L. Cao, B. Shi, Z. Zhang, C. Tongsh, K. Jiao, K. Zhu, Z. Jiang, *Adv. Mater.* **2020**, *32*, 2001284.

[50] W. Xin, Z. Zhang, X. Huang, Y. Hu, T. Zhou, C. Zhu, X.-Y. Kong, L. Jiang, L. Wen, *Nat. Commun.* **2019**, *10*, 3876.

[51] C. Lee, L. Joly, A. Siria, A.-L. Biance, R. Fulcrand, L. Bocquet, *Nano Lett.* **2012**, *12*, 4037.

[52] W.-L. Huang, X.-D. Wang, Y.-F. Ao, Q.-Q. Wang, D.-X. Wang, *J. Am. Chem. Soc.* **2020**, *142*, 13273.

[53] W. Sparreboom, A. Van den Berg, J. C. T. Eijkel, *Nat. Nanotechnol.* **2009**, *4*, 713.